

Evidence for bathymetric control on the distribution of body wave microseism sources from temporary seismic arrays in Africa

Garrett G. Euler,^{1*} Douglas A. Wiens¹ and Andrew A. Nyblade²

¹*Department of Earth and Planetary Sciences, Washington University in St. Louis, Campus Box 1169, One Brookings Drive, St. Louis, MO 63130-4862, USA. E-mail: ggeuler@lanl.gov*

²*Department of Geosciences, Penn State, 441 Deike Building, University Park, PA 16802, USA*

Accepted 2014 March 18. Received 2014 February 15; in original form 2013 September 26

SUMMARY

Microseisms are the background seismic vibrations mostly driven by the interaction of ocean waves with the solid Earth. Locating the sources of microseisms improves our understanding of the range of conditions under which they are generated and has potential applications to seismic tomography and climate research. In this study, we detect persistent source locations of *P*-wave microseisms at periods of 5–10 s (0.1–0.2 Hz) using broad-band array noise correlation techniques and frequency-slowness analysis. Data include vertical component records from four temporary seismic arrays in equatorial and southern Africa with a total of 163 broad-band stations and deployed over a span of 13 yr (1994–2007). While none of the arrays were deployed contemporaneously, we find that the recorded microseismic *P* waves originate from common, distant oceanic bathymetric features with amplitudes that vary seasonally in proportion with extratropical cyclone activity. Our results show that the majority of the persistent microseismic *P*-wave source locations are within the 30–60° latitude belts of the Northern and Southern hemispheres while a substantially reduced number are found at lower latitudes. Variations in source location with frequency are also observed and indicate tomographic studies including microseismic body wave sources will benefit from analysing multiple frequency bands. We show that the distribution of these source regions in the North Atlantic as well as in the Southern Ocean correlate with variations in bathymetry and ocean wave heights and corroborate current theory on double-frequency microseism generation. The stability of the source locations over the 13-yr time span of our investigation suggests that the long-term body wave microseism source distribution is governed by variations in the bathymetry and ocean wave heights while the interaction of ocean waves has a less apparent influence.

Key words: Interferometry; Body waves; Africa; Atlantic Ocean; Indian Ocean.

1 INTRODUCTION

The primary motivations for studying microseisms are to provide information useful for seismograph site selection (e.g. Peterson 1993; McNamara & Buland 2004), imaging the Earth structure (Sabra *et al.* 2005; Benson *et al.* 2007; Yang & Ritzwoller 2008; Lin *et al.* 2008, 2009; Prieto *et al.* 2009; Tsai 2009; Harmon *et al.* 2010; Zhang *et al.* 2010b; Lawrence & Prieto 2011; Lin & Ritzwoller 2011; Lin *et al.* 2012a,b), monitoring geological structures (Sens-Schönfelder & Wegler 2006; Wegler & Sens-Schönfelder 2007; Brenguier *et al.* 2008a,b) and climate (Aster *et al.* 2008, 2010; Stutzmann *et al.* 2009; Grob *et al.* 2011). Arrays of seismometers can be used to filter the

wave energy by slowness (the inverse of velocity), azimuth and frequency (Burg 1964; Capon 1969; Lacoss *et al.* 1969; Rost & Thomas 2002, 2009), thus providing a powerful approach to the study of microseisms. Array analysis of microseism properties has focused on surface wave sources (Ramirez 1940a,b; Haubrich & McCamy 1969; Capon 1973; Cessaro & Chan 1989; Cessaro 1994; Friedrich *et al.* 1998; Schulte-Pelkum *et al.* 2004; Shapiro *et al.* 2006; Stehly *et al.* 2006; Chevrot *et al.* 2007; Obrebski *et al.* 2012, 2013) and compressional body wave sources (Toksöz & Lacoss 1968; Haubrich & McCamy 1969; Gerstoft *et al.* 2006, 2008; Koper & de Foy 2008; Zhang *et al.* 2009; Koper *et al.* 2009, 2010; Landes *et al.* 2010; Zhang *et al.* 2010a; Obrebski *et al.* 2013). While many of these studies have inferred that surface wave microseisms observed on continents are primarily generated from ocean wave action near coastlines, recent studies using polarization analysis provide evidence for an open ocean origin (Kedar *et al.* 2008; Stutzmann *et al.*

*Now at: Geophysics Group, Earth and Environment Sciences Division, Los Alamos National Lab, Los Alamos, NM 87545, USA.

2009; Obrebski *et al.* 2012, 2013). In contrast, there is consensus among studies of compressional body wave microseisms that these waves originate near the wind source. This potential distinction between surface and body wave microseism provenance can lead to large differences in the distribution of the two wave types as ocean waves may travel thousands of kilometres from the storm centre (the wind source) to a coastline.

Microseisms created by the action of ocean waves produce two broad peaks in the Earth's background spectra and are classified as either single-frequency (SF) or double-frequency (DF) microseisms depending on the mechanism of generation (Longuet-Higgins 1950; Haubrich *et al.* 1963; Hasselmann 1963; Webb 1992; Bromirski & Duennebieber 2002; Tanimoto 2007; Webb 2008; Ardhuin *et al.* 2011, 2012; Ardhuin & Herbers 2013). While both SF and DF surface wave microseisms are regularly observed, only DF body wave microseisms have been conclusively detected (e.g. Haubrich & McCamy 1969) although a recent effort to detect teleseismic body waves in the frequency range of SF microseisms has been made (Landes *et al.* 2010). Recent studies (Bromirski *et al.* 2005; Tanimoto 2007; Zhang *et al.* 2010a) have further differentiated the DF microseisms into two subclasses: long-period double-frequency (LPDF) and short-period double-frequency (SPDF). This division arises because the source locations of these two subclasses are often distinct, due to the greater attenuation of ocean swell from distant storms at SPDF frequencies than at LPDF frequencies. This increased attenuation of higher frequency ocean waves also gives rise to a strong correlation of SPDF microseisms with wind activity near the source location (Bromirski *et al.* 2005; Zhang *et al.* 2009).

Within a few years of the first identification of microseismic body waves (Backus *et al.* 1964), studies found these waves mostly originated near storms over the ocean and often from storms moving faster than the storm-wind-generated ocean waves (Toksöz & Lacoss 1968; Lacoss *et al.* 1969; Haubrich & McCamy 1969). After three decades with little further study, interest in microseismic *P* waves returned (e.g. Gerstoft *et al.* 2006) as tomographic imaging with Rayleigh wave microseisms became routine practice (e.g. Benson *et al.* 2007). The identification of microseismic body waves generated from distant storms that penetrate the Earth's core has been recently reported numerous times (Gerstoft *et al.* 2008; Koper & de Foy 2008; Koper *et al.* 2009, 2010; Landes *et al.* 2010) and better establishes storms as candidates for seismic data in tomographic studies. Several studies have also noted that long-term averages of microseism data from arrays in North America and Asia identify sources of compressional body wave microseisms coming from regions of increased ocean wave activity (Gerstoft *et al.* 2008; Landes *et al.* 2010; Zhang *et al.* 2010a). In particular, most of these regions lie within the 30–60° latitude range dominated by large maritime storms known as extratropical cyclones. These storm systems constantly sweep across the mid-latitude band of the Northern and Southern hemispheres and differ significantly in structure from the tropical cyclones that occur at low latitudes (Wallace & Hobbs 2006). Because extratropical cyclone systems are strongly linked to the energy budget of the atmosphere through the Lorenz Energy Cycle (Lorenz 1955), they are likely influenced by climate change (e.g. Bengtsson *et al.* 2009) and potentially generate climate signals recoverable from the analysis of the body wave microseism spectrum.

In this study, we infer the seasonal distribution of microseismic body waves propagating through several regional broad-band arrays in equatorial and southern Africa utilizing noise correlation techniques and frequency-slowness analysis. Although the arrays were not operated simultaneously, combining observations as a

function of month allows us to infer general properties of the seasonal microseism spectra in Africa. Our focus is on the properties of compressional body wave microseism sources in two period bands: an SPDF band (5–7.5 s) and an LPDF band (7.5–10 s). We find evidence for several common, stable locations supporting that body wave microseisms produced by the interaction of opposing ocean wavefields are enhanced by bathymetry (Longuet-Higgins 1950; Tanimoto 2007; Kedar *et al.* 2008; Ardhuin *et al.* 2011; Ardhuin & Herbers 2013). We also show that the majority of body wave microseism observations are linked to the latitude ranges (30–60°) and seasonality of extratropical cyclone activity.

2 DATA

Observations of compressional body wave microseisms have used arrays in North America (Toksöz & Lacoss 1968; Haubrich & McCamy 1969; Lacoss *et al.* 1969; Gerstoft *et al.* 2006, 2008; Koper *et al.* 2009; Zhang *et al.* 2009, 2010b), Asia (Koper & de Foy 2008) or on both continents (Landes *et al.* 2010; Zhang *et al.* 2010a) with one notable exception at short periods (Koper *et al.* 2010). Africa provides a convenient landmass to study microseisms in that it extends from the northern equatorial regions into the Southern Hemisphere, thus providing constraints and comparisons on noise generation in both hemispheres, including the largely oceanic Southern Hemisphere. We chose to use four arrays deployed in equatorial and southern Africa over a 13-yr time span (Fig. 1). For the remainder of this study we refer to the arrays as the Cameroon, Ethiopia, South Africa and Tanzania arrays when we need to distinguish between them. In the following sections we provide a short description of each array.

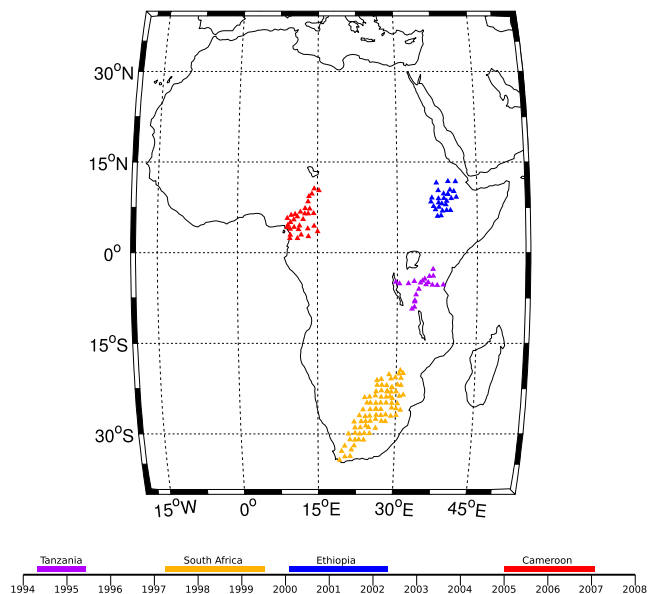


Figure 1. Location and deployment times of the broad-band seismometer arrays in this study. There are four arrays consisting of the 32-station Cameroon array (red triangles, deployed from 2005 January to 2007 January), the 28-station Ethiopia array (blue triangles, deployed from 2000 February to 2002 May), the 21-station Tanzania array (purple triangles, deployed from 1994 May to 1995 June) and the 82-station South Africa array (yellow triangles, deployed from 1997 April to 1999 July).

2.1 Tanzania

The Tanzania Broadband Seismic Experiment has the fewest seismometers, the shortest duration and the earliest deployment of the arrays in our study. The array consists of 21 broad-band stations deployed from 1994 May to 1995 June in two lines forming a cross pattern intersecting near the middle. The linear components have 11 seismic stations spaced about 100 km apart with one line oriented roughly east–west and the other northeast–southwest. The seismic equipment consisted of a Streckeisen STS-2 (G. Streckeisen & Co., Pfungen, Switzerland) or Güralp CMG-3ESP (Güralp Systems Ltd., Reading, UK) seismometer linked to a REF TEK RT72A-08 digital recorder (Refraction Technology, Inc., Plano, TX, USA) sampling at 20 and 1 Hz. The experiment has been used to image the structure of the Archean Tanzania Craton and the terminus of the East African Rift in northern Tanzania using local, regional and teleseismic earthquakes (e.g. Nyblade *et al.* 1996; Weeraratne *et al.* 2003; Julià *et al.* 2005).

2.2 South Africa

The Southern Africa Broadband Seismic Experiment is the most instrumented array in our study with 82 broad-band sites deployed from 1997 April to 1999 July. The array has been successfully used to image the Archean Kaapvaal and Zimbabwe Cratons, the surrounding Proterozoic provinces, and the underlying mantle using teleseismic earthquakes and seismic noise (e.g. James *et al.* 2001, 2003; Fouch *et al.* 2004; Yang *et al.* 2008). The array comprised 32 fixed stations and a 23-station mobile component that occupied another 50 sites over the 2-yr deployment. The sites were spaced at roughly 100 km intervals in a fairly regular grid with lines oriented north–south and east–west and a total aperture of approximately 2000 km in the northeast–southwest direction and 700 km in northwest–southeast direction. Instrumentation included Streckeisen STS-2 and Güralp CMG-3 seismometers digitized at 20 Hz which we decimated to 1 Hz for our analysis.

2.3 Ethiopia

The Ethiopia Broadband Seismic Experiment utilized 38 broad-band stations deployed between 2000 March and 2002 March. Data from the array have been used to image the crustal and upper-mantle structure of the East African Rift and surrounding plateaus using local, regional and teleseismic earthquakes and seismic noise (Nyblade & Langston 2002; Dugda *et al.* 2005; Bastow *et al.* 2008; Kim *et al.* 2012). We removed 10 stations from the original 38-station Ethiopia array as these sites formed a separate subarray located 700 km to the south in Kenya. During the first year of the experiment only six seismic stations were operational in Ethiopia while an additional 22 stations were installed in the region for the second year. The aperture of the Ethiopia array was about 550 km east–west and 700 km north–south with an irregular spacing of 50–200 km to optimize 3-D seismic imaging at mantle depths. Stations comprised either a Güralp CMG-3, CMG-3T, CMG-40T or Streckeisen STS-2 seismometer that was digitally recorded at 20 and 1 Hz.

2.4 Cameroon

The Cameroon Broadband Seismic Experiment was deployed between 2005 January to 2007 January with a design goal of 3-D imaging the structure of the continental portion of the Cameroon Volcanic Line and the northern limit of the Congo Craton using tele-

seismic earthquakes (Reusch *et al.* 2010; Tokam *et al.* 2010; Reusch *et al.* 2011; Koch *et al.* 2012). The experiment started with eight pilot stations for the first year and was expanded to 32 stations for the remaining year. The array aperture varied from a maximum of over 1000 km in the northeast–southwest direction to a minimum of just over 600 km in the northwest–southeast direction. The stations extend throughout the country of Cameroon and were spaced unevenly at 50–200 km intervals to optimize imaging at mantle depths using body waves and surface waves. Each station consisted of a Streckeisen STS-2, Güralp CMG-3T or Güralp CMG-3ESP with a REF TEK RT130 digital recorder sampling at 40 and 1 Hz.

3 METHODS

3.1 Isolation of microseisms

One method of studying the seasonal characteristics of seismic noise is to correlate months-long seismic records to produce noise correlation functions (NCFs) that summarize the spatially coherent noise field between pairs of stations. Previous studies have noted the equivalence of NCFs from correlating long time sections with those produced by averaging the correlations of smaller time sections (e.g. Benson *et al.* 2007; Seats *et al.* 2012), a power spectrum feature originally exploited by Welch (1967). We take advantage of this approach by dividing 1 Hz vertical component recordings into 25-hr windows with overlap during the first hour of each day. This provides a seamless correlation of data across day boundaries with only minor data repetition. A side-effect of using time windows of this length is that most windows include earthquake waveforms that may bias the results. To suppress the earthquake waveforms in the records we utilize techniques intended for ambient noise tomography (Benson *et al.* 2007) while other studies average correlations of shorter time windows to suppress earthquakes (e.g. Gerstoft & Tanimoto 2007). We summarize below these additional data processing steps on individual records in our study.

After windowing, records with no amplitude variation or those with data from less than 75 per cent of the 25-hr window were removed to avoid bias from significant instrumental problems. The records were then detrended, tapered and converted to displacement. Next, both time-domain and frequency-domain normalization was implemented to force the energy ratio of earthquakes and microseisms to the relative proportions that the two represent in time. In our study region and for all previous studies of microseisms that we are aware of, time periods with only microseismic noise far outnumber those with earthquakes waveforms. In this way, normalization leads to earthquake energy having little influence on the seismic noise field (e.g. Toksöz & Lacoss 1968). Our temporal normalization utilized a two-pass sliding absolute mean. The first pass normalization utilized a 75-s sliding window of the unfiltered records to suppress the effect of automatic recentring of seismometer masses. The second pass normalization was tuned to the earthquake band (15–100 s) as in Benson *et al.* (2007). The last normalization step, spectral whitening, was implemented by dividing the complex spectra with a smoothed version of the amplitude spectra generated with a 2-mHz-wide sliding mean. The normalized records were then cross-correlated for each unique station pair in every 25-hr window. These correlograms were cut between –4000 and 4000 s in lag time to save space without affecting the coherent signal between the stations. Finally, the NCF data were generated by stacking correlograms for each station pair across each month independent of year. For example, a January stack for a station pair

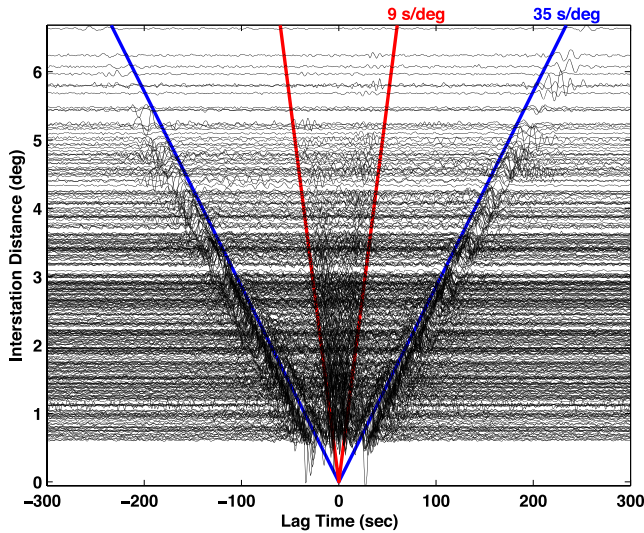


Figure 2. Plot of noise correlations from station pairs in the Ethiopia array as a function of station pair separation. The noise correlations are 2-yr stacks (the entire deployment time of the array). Arrivals in positive (causal) time correspond to correlated noise propagating through the source station before the receiver station, while negative (acausal) time indicates the noise arrives at the receiver station first. The waves with slowness near 35 s deg^{-1} (corresponding to a group velocity of about 3.2 km s^{-1}) are the Rayleigh waves of the partially recovered two-way Green's function of the Earth between each station pair. The arrivals with moveouts higher than 9 s deg^{-1} represent teleseismic body waves consistently arriving from specific abyssal locations and are not part of the interstation Green's function.

in the Cameroon array may include correlations from January of 2005, 2006 and 2007. In Fig. 2 we show NCFs from stacking correlograms for the entire deployment time of the Ethiopia array as the body wave microseisms, which travel at lower slownesses than surface wave microseisms, are visible at lag times corresponding to slownesses below 9 s deg^{-1} .

3.2 Frequency–slowness spectra

To understand the seasonal properties of microseisms propagating through each array, we used a conventional frequency–wavenumber (f – k) approach to estimate the frequency–slowness power spectrum (hereafter referred to as the f – s spectrum; Lacoss *et al.* 1969). The f – s spectrum gives the distribution of seismic wave power as a function of frequency, slowness and direction of propagation through an array. This approach assumes the wavefield is both stationary in space and time implying that the second-order statistics do not vary significantly for a set of our 25-hr recordings of an array. We expect this assumption is valid as the individual arrays in this study do not span one or more continents or include ocean-bottom stations and so the microseisms are unlikely to attenuate significantly across an array or differ significantly in their characteristics. In the conventional approach, the f – s spectrum is estimated by frequency-domain delay and sum of cross power spectra over a range of slowness vectors. The power of the array for an individual slowness and frequency is expressed as:

$$P(f, s) = \frac{1}{N^2} \sum_{i=1}^N \sum_{j=1}^N w'_i w_j C_{ij}(f) e^{-i2\pi f s (x_j - x_i)}, \quad (1)$$

where w_i and w_j are station weights, C_{ij} is the cross-spectra between stations i and j , s is the slowness vector in the direction of the wave source and $x_j - x_i$ is the spatial difference vector for the station pair.

The $'$ symbol denotes complex conjugation. We normalize the cross spectra using each record's power spectra to give the coherency of the wavefield between a pair of stations at a particular frequency:

$$C_{ij}(f) = \frac{S'_i(f) S_j(f)}{\sqrt{S'_i(f) S_i(f) + S'_j(f) S_j(f)}}. \quad (2)$$

Because correlograms are the time-domain representation of the cross power spectrum between a pair of stations, converting our NCFs to the frequency-domain gives the individual elements of the cross-spectral matrix \mathbf{C} . We limited our NCFs to unique station pairs and did not include autocorrelations which means our estimation of the f – s spectrum is reduced to a summation over half of the off-diagonal elements of \mathbf{C} . This modifies (1) to a summation over pair indices rather than station indices:

$$P(f, s) = \frac{1}{N} \sum_{p=1}^N w_p \frac{C_p(f)}{|C_p(f)|} e^{-i2\pi f s x_p}, \quad (3)$$

where we have also combined the individual station weight and location terms. This reformulation halves the slowness spectrum computation while improving the beam resolution (Westwood 1992). A disadvantage of this approach is it prevents us from using more sophisticated high-resolution f – s spectra estimations that require inversion of the cross-spectral matrix (e.g. Capon 1969) but these have been shown to give similar results to the conventional approach for statistical studies of microseisms (Koper *et al.* 2010).

We then average the f – s spectra computed above over frequency to simplify our analysis to SPDF and LPDF sources:

$$P_{\text{SPDF}}(s) = \frac{1}{M_1} \sum_{f=\frac{1}{7.5\text{s}}}^{\frac{1}{5\text{s}}} P(f, s), \quad (4)$$

$$P_{\text{LPDF}}(s) = \frac{1}{M_2} \sum_{f=\frac{1}{10\text{s}}}^{\frac{1}{7.5\text{s}}} P(f, s). \quad (5)$$

M_1 and M_2 are the number of discrete frequencies over which the f – s spectra are summed in the SPDF and LPDF bands, respectively. These two bands represent a large frequency range that potentially may hide narrow band microseism sources in lieu of those with a greater bandwidth. Equivalently, sources that are short-lived will also have less power in the spectra compared to those that are persistent throughout the time span of an individual spectrum (1 month). Therefore, our f – s spectrum estimates give the distribution of microseisms as a function of slowness, azimuth and frequency where the power is a product of microseismic source coherency across the array, time persistence and frequency bandwidth.

The spatial arrangement of elements within an array has a substantial effect on the estimation of the f – s spectrum of the microseisms passing through that array (e.g. Haubrich 1968). In an ideal case, to perfectly resolve the propagating waves under the array requires an infinite number of stations that completely sample the waves spatially. While all arrays are far from this ideal, some represent a pragmatic compromise in spectral resolution for a significant reduction in the number of stations. One of the best ways to understand how well an array may estimate the true microseism f – s spectrum is to compute the array response function (ARF) for a single plane wave:

$$\text{ARF}(f, s) = \frac{1}{N} \sum_{p=1}^N w_p e^{-i2\pi f (s-s_0) s_p}, \quad (6)$$

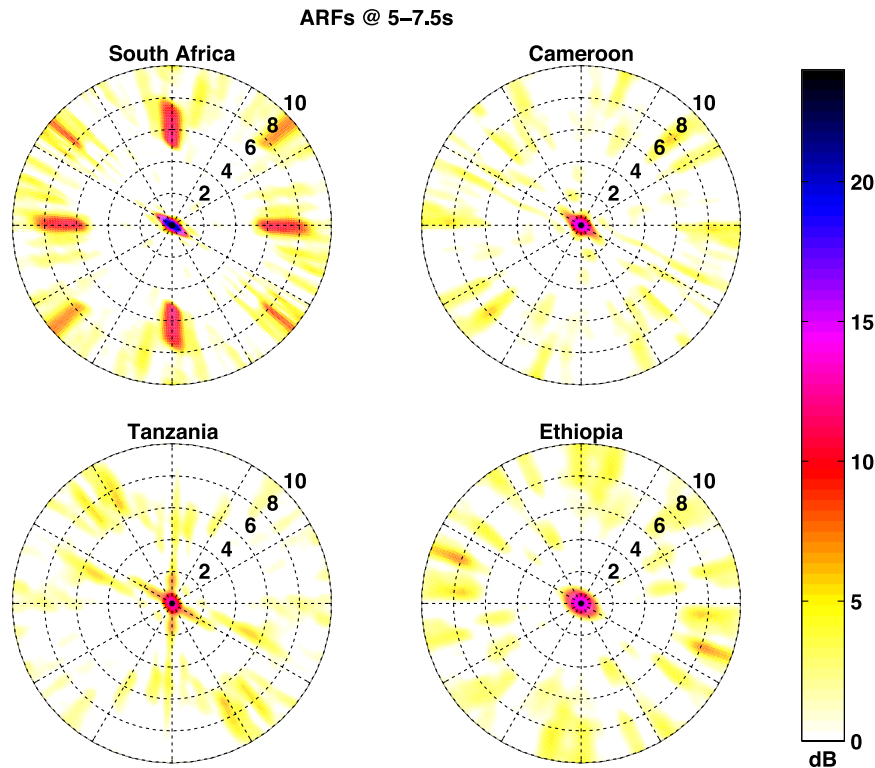


Figure 3. Array response function (ARF) for each array averaged over the 546 frequencies (spaced at 0.000122 Hz) from the Fourier transform of the corresponding data in the period band of 5–7.5 s. These ARFs are the slowness resolution of the arrays to a plane wave with unit spectral amplitude over the period band 5–7.5 s and zero slowness (the equivalent of a vertically incident plane wave). The slowness resolution for an incident 5–7.5 s period P wave is a shift of these ARF images from zero slowness to the corresponding slowness of the P wave. The slowness resolution for the 7.5–10 s band (containing 273 Fourier frequencies) is not shown here but is similar with an enlargement of the features proportional to the ratio of the two period bands. Each response is normalized to give 0 dB at the median value and clipped to the range of 0–24 dB. This emphasizes the features of the main peak and as well as subtle slowness aliasing such as the grating lobes of the South Africa ARF.

where (6) is equivalent to (3) when the cross spectral elements C are set to unity and s_0 is the slowness vector of the plane wave propagating through the array. The ARF shows the slowness aliasing pattern (spectral resolution) of the array for that wave. We computed the array response for waves incident on each array with a slowness of 0 s deg^{-1} over the SPDF frequency band to highlight the aliasing features (Fig. 3). The averaging over frequency smears aliasing features such as grating lobes because the slowness of the lobes varies with frequency (Rost & Thomas 2002). In strong contrast to the grating lobes is the central peak, corresponding to the correct slowness of the propagating wave, that is enhanced by the averaging because its slowness does not change with frequency.

All of the arrays in our study have similar station spacing but variations in the number of stations, their arrangement and the overall aperture result in distinct array responses. The number of stations in an array affects the signal-to-noise ratio of the central lobe, the arrangement determines the grating lobe locations and the aperture of an array is directly related to the sharpness of the central lobe (Rost & Thomas 2002). For example, the Tanzania array is a 21-station, cross-shaped array with a maximum aperture of 900 km while the Ethiopia array consists of 28 clustered stations with a maximum aperture of 750 km. Comparing the responses of the two arrays in Fig. 3 shows that while the central lobe of the Tanzania array response is actually sharper due to the array's wider aperture, there is substantial anisotropy of the central lobe width due to the cross-shape of this array. The Ethiopia response has a well-developed central peak with no significant grating lobes within

30 s deg^{-1} . The overall background level of the response is also higher for the Tanzania array due to the fewer number of stations (Ethiopia has 28 while Tanzania has 21) resulting in a lower signal-to-noise ratio of the central lobe. The 7.5–10 s spectral band has similar array responses to that at the short periods but the spectral features are enlarged as array response scales linearly with period. This has a result of moving the rather significant grating lobes in the ARF of the South African array farther from the central lobe at longer periods.

3.3 Backprojection of frequency–slowness spectra

In our analysis, slowness in the f – s spectrum is related to a unique ray path and distance for a given phase (Figs 4a and b). This allows backprojection of the f – s spectrum over a range in slowness to a range in distance for a particular body wave phase (Haubrich & McCamy 1969). Some of the body wave energy in these slowness ranges also propagates as phases other than P , PP & PKP , but these are not anticipated to be as energetic as pointed out by Gerstoft *et al.* (2008) and so we did not explore backprojection of those phases. Slownesses are matched to a phase ray path using the 1-D earth model AK135 (Kennett *et al.* 1995) and combined with the backazimuth to give an estimate of the originating location of the body wave energy relative to the array centre. For example, we projected the f – s spectrum of the NCFs stacked over the entire deployment of the Ethiopia array (Fig. 2) in the slowness

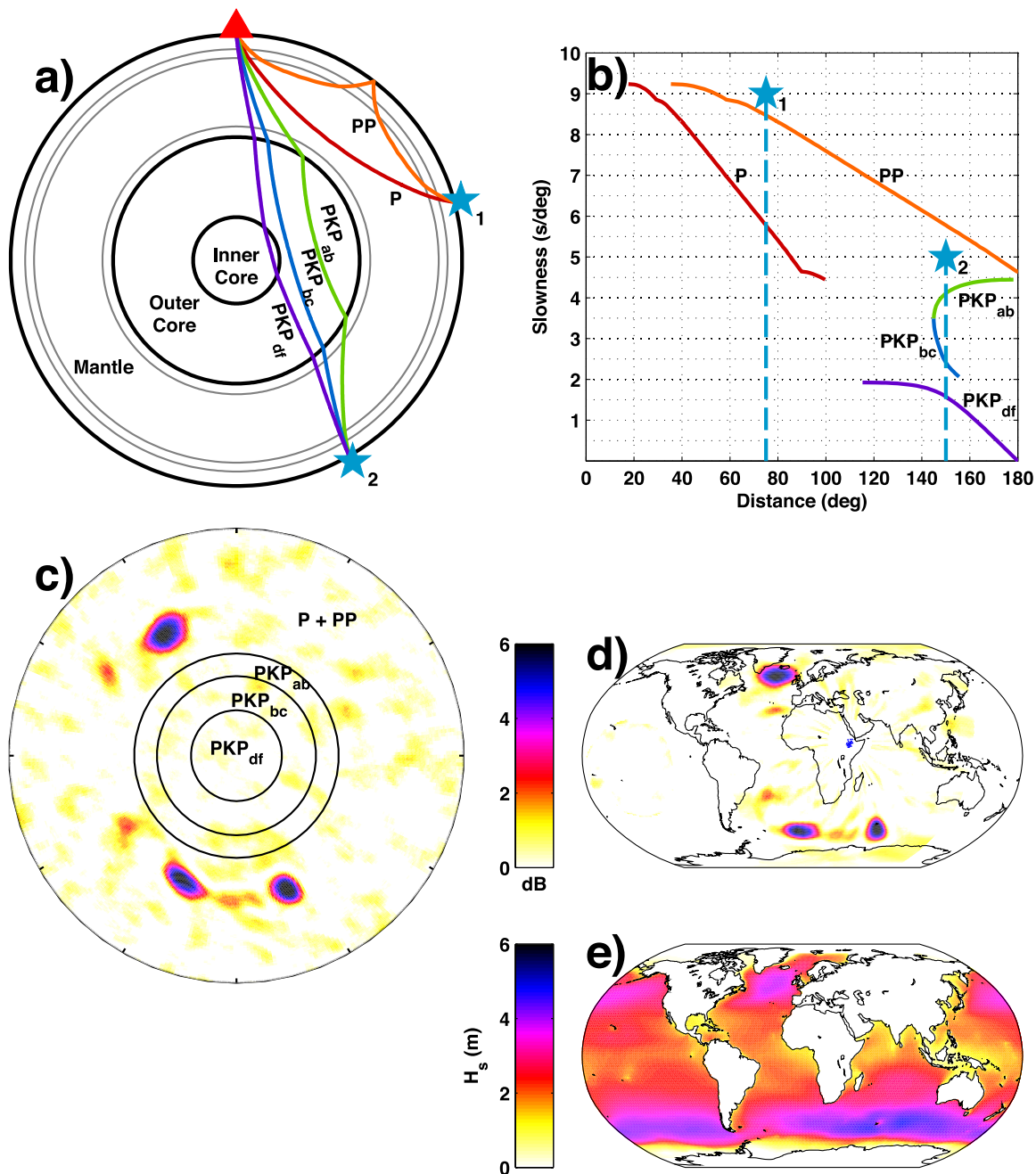


Figure 4. Plot illustrating the method of backprojecting body wave seismic noise recorded by the Ethiopia array to estimate source locations. (a) Example ray paths of microseismic body wave phases expected to have the highest amplitudes (Astiz *et al.* 1996; Gerstoft *et al.* 2008). (b) Plot of the slowness versus distance relationship of those seismic phases for a surface source propagating through the 1-D earth model AK135 (Kennett *et al.* 1995). The overlap in slowness of P & PP introduces a distance ambiguity for waves recorded in the slowness range of $4.5\text{--}9.25\text{ s deg}^{-1}$. For example, waves travelling through the array at 7.5 s deg^{-1} may be interpreted as P waves from a source 50° from the array and PP waves from a source at a 100° distance range. We do not include the P & PP slowness curves above 9.25 s deg^{-1} in our analysis as triplications in these phases further complicate the slowness to distance relationship. (c) Slowness spectrum for the noise correlations in Fig. 2 averaged across the $5\text{--}7.5\text{ s}$ period band. The spectrum is divided by concentric black rings at 2.0 , 3.5 and 4.5 s deg^{-1} corresponding to the slowness ranges of the different seismic phases shown. The spectrum is normalized to give 0 dB at the median value. (d) P & PKP_{bc} backprojection of the slowness spectrum using the slowness–distance curves. (e) Significant wave height hindcasts (Tolman 2009) averaged from 2000 February to 2002 May (the Ethiopia array deployment duration) show that the backprojected seismic noise recorded by the Ethiopia array is strongest where there is substantial ocean wave activity.

ranges of P and PKP_{bc} as they do not overlap in distance and are expected to be higher in amplitude compared to the other phases in this study (Figs 4b–d). The backprojected Ethiopia f – s spectrum indicates that the North Atlantic between Greenland and Iceland is a significant source of P waves as well as two other regions in the

Southern Hemisphere. Hindcasts of significant ocean waveheights (Tolman 2009) averaged over the same time span show two main belts of high seas between 30° and 60° latitude (Fig. 4e) overlapping with the backprojection locations. This provides confidence that the body waves are P waves and not PP waves as the backprojection of

P-Wave ARFs @ 5–7.5s

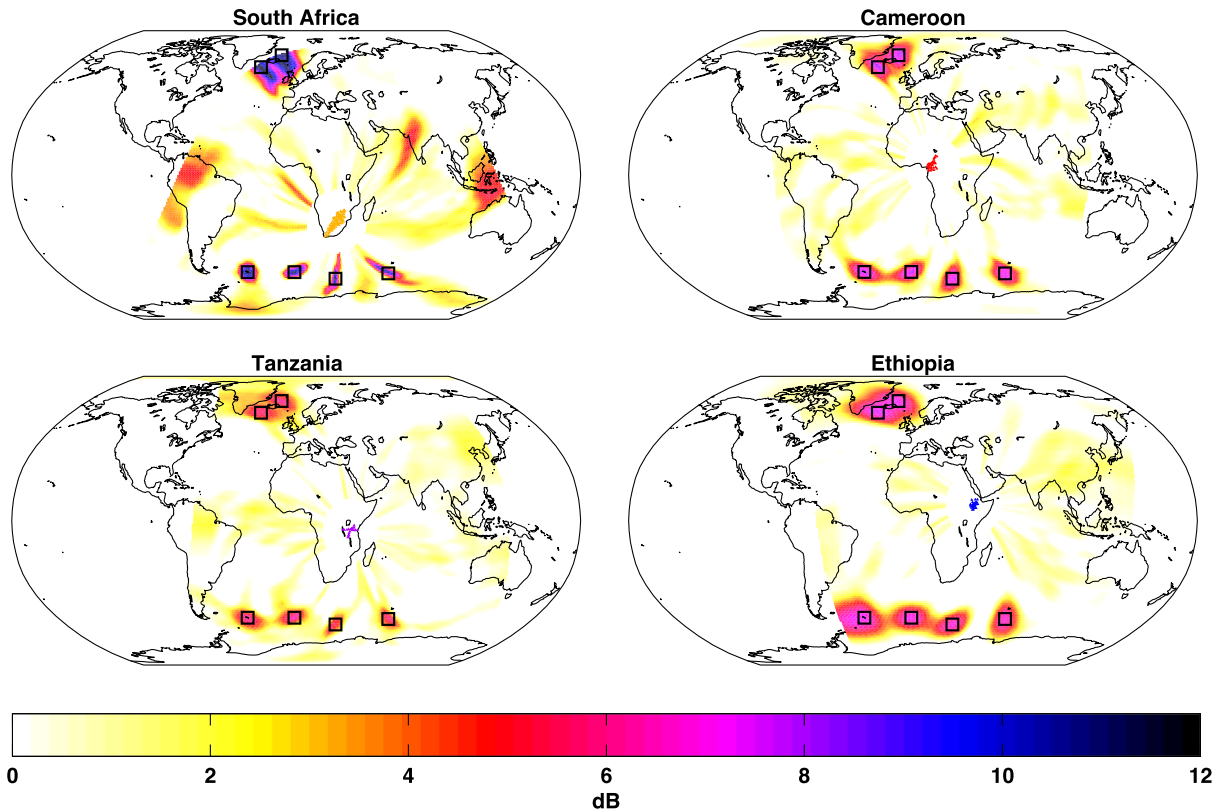


Figure 5. Backprojection ARFs for hypothetical source locations (black boxes) of microseismic P waves at each array in this study showing the source location resolution for the 5–7.5 s period band. Each array has the stations coloured as from Fig. 1. The responses are created for each array by offset of the ARFs from Fig. 3 to the corresponding slowness for P waves from the source locations, averaging these offset ARFs for the six source locations, and then backprojecting this average. The result is normalized to give 0 dB at the median value.

the f - s spectrum assuming PP -wave propagation places the three sources in the central Pacific Ocean where wave heights are comparably lower. Direct comparison of backprojected f - s spectra to significant wave heights (a measurement of the ocean wave amplitude) is not straightforward as DF microseisms are generated by the interference of ocean waves and are modulated by the ocean depth as well as wave heights (Longuet-Higgins 1950; Arduin & Herbers 2013). Modelling of the ocean wavenumber spectrum directly shows the intensity of interference of ocean waves and provides a more appropriate tool for relating body wave microseisms propagating beneath arrays to the activity of ocean waves and storms (Kedar *et al.* 2008; Arduin *et al.* 2011, 2012; Obrebski *et al.* 2012, 2013). However, in this study we make inferences based only on maps of significant wave height and bathymetric excitation. We suggest that together these alternatives provide a realization of the DF microseismic spectrum without estimation of the ocean wavenumber spectrum assuming wave–wave interference of the ocean is spatially and directionally random over the timescales in our study. We note that the strong geographic correspondence of a year-long average of ocean-bottom pressure estimated from ocean wavenumber spectra by Arduin *et al.* (2011) (see their fig. 7a) and long averages of significant wave height, such as shown in Fig. 4(e) of this study, lend support to our approach.

The interpretation of backprojection f - s spectra is limited by the slowness resolution of the corresponding array. For example, if an array has a low resolution because of a small aperture then it is difficult or impossible to determine the number, location and

geometry of the microseism sources. Aliasing features such as grating lobes further degrade resolution. To understand the resolution of the arrays in this study, we computed multiplanewave ARFs for each array corresponding to P waves originating from several oceanic locations. These were constructed by averaging the ARFs for the different locations and then backprojecting the result (Fig. 5). For the SPDF band of 5–7.5 s shown in Fig. 5, all backprojection P -wave source locations match the expected locations with no discernible aliasing at other locations.

At LPDF periods, the slowness resolution of several arrays begins to be too low to resolve neighbouring P -wave source locations. In this case the responses of the sources merge and appear as a single source around the average location. For instance, only the South Africa array is able to accurately separate the two North Atlantic source locations in the LPDF band while the other three arrays inaccurately indicate Iceland as the sole source location. The Ethiopia array resolution is also nearly too low to distinguish the Southern Hemisphere source locations while in contrast, the South Africa array resolution is such that the spectrum is nearly undersampled by a 1° step-size. The computation of backprojection ARFs are also useful for evaluating the dimensions of a source region by comparing the observed f - s spectra to the point source resolution at the source regions. For example, the main source regions of 5–7.5 s P -wave microseisms observed by the Ethiopia array (Fig. 4d) are different than the 5–7.5 s backprojection ARFs in the same locations in Fig. 5. The differences indicate that there is no distinct second source to the north while in

the south the regions are significantly broader than that of a point source.

3.4 Combining microseism observations from multiple arrays

Because every array has a different response to propagating waves (Rost & Thomas 2002), combining the f - s spectra from multiple arrays is not a straightforward task. Instead we created a graphical interface to allow an analyst to pick peaks in a spectrum. These picks provide a simple representation of the microseismic body waves traversing an array and we use them to combine and summarize the f - s spectra from all the arrays in order to look for common sources. We selected as many peaks as necessary to represent the main features of the f - s spectrum (Fig. 6). We defined these main features as peaks that are 2 dB above the median of the spectrum but exceptions (down to 1.8 dB) were made for the South Africa and Tanzania arrays as we found their spectral features were often weaker, possibly due to signal loss associated with aliasing and array aperture. While this approach does introduce some subjectivity, we felt it the most pragmatic method to avoid the detrimental effects of slowness aliasing that would otherwise hinder a more automated analysis. Other studies analysing more slowness spectra include only the maximum of each spectrum to similarly avoid bias from aliased features (e.g. Koper *et al.* 2009, 2010).

Location errors larger than the width of the continental shelf have the potential to significantly alter interpretation of microseism generation near distant coastlines. While there are a number of studies that have located microseismic body wave sources, none to our knowledge have attempted to estimate the effect of 3-D seismic velocity structure on the apparent locations. Such an investigation is straightforward as methods have been devised for earthquake waveforms (e.g. Nolet 2008). We perform a simple investigation into the effect of 3-D velocity structure on our apparent source locations assuming the 3-D structure of Crust1.0 (Laske *et al.* 2013) and HMSL-P06 (Houser *et al.* 2008).

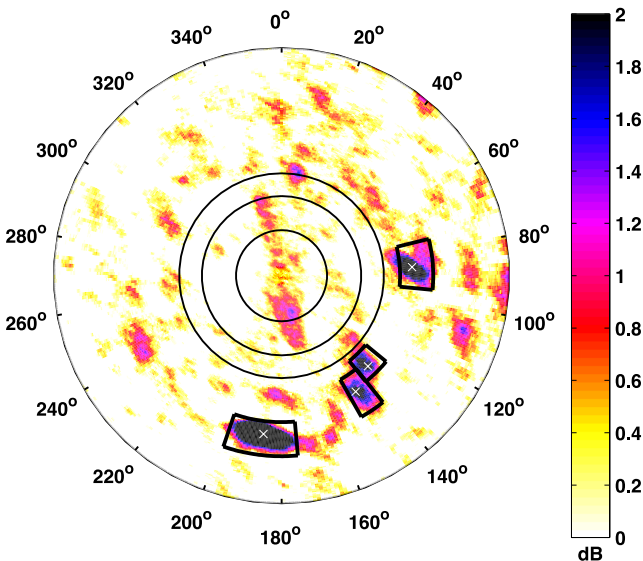


Figure 6. Peaks picked for the Cameroon array June f - s spectrum averaged over 7.5–10 s periods. An analyst picks a peak (white X's) by selecting the local slowness-azimuth space (black boxes). Concentric black rings denote seismic phase slowness ranges from Fig. 4(c). The spectrum is normalized to give 0 dB at the median value.

To find the effect of the 3-D velocity heterogeneity, we first generate ray paths through the 1-D mantle model AK135 between each station in the array and an apparent source location. We then accrue a travel time perturbation for each ray path using Fermat's principle (Nolet 2008). Perturbations due to ellipticity are also included (Kennett & Gudmundsson 1996). We then performed a linear least-squares fit to the traveltimes perturbations for an array as a function of either north or east position. This gives the slowness bias of the 3-D heterogeneity in terms of seconds per degree north and east. This bias is then removed from the original slowness measurement to get a corrected slowness. Backprojection of the new slowness gives a better estimate of the source location if the Earth structure is appropriately represented by the velocity models and assuming the bias factors do not change significantly over the scale lengths of the location correction. The typical values of these slowness corrections and their effect on the backprojected locations are discussed in the results section.

4 RESULTS

4.1 Backprojection spectra

Backprojection maps for January and June f - s spectra (Fig. 7) illustrate the seasonal differences of P -wave microseisms originating from the Northern and Southern hemispheres. In January, every array detects microseisms that appear to originate in the North Atlantic region south of Iceland and west of Greenland (hereafter SI). The averaged significant wave height hindcast (Tolman 2009) for the month of 2001 January shows the SI region is associated with consistently strong ocean wave activity. Another apparent source of January P -wave microseisms observed in Tanzania appears to be located in West Africa. These microseisms are most likely PP waves from the SI region which bounce beneath West Africa as atmospheric disturbances over land do not generate significant P waves (Hasselmann 1963) and low-frequency cultural noise is rare and has not been observed at teleseismic distances (e.g. Sheen *et al.* 2009).

Two of the arrays (Cameroon and Tanzania) also find P -wave microseisms originating from near the northern coast of Iceland (NI). The January significant wave height map shows that this region is near strong wave heights and it is likely that the averaged significant wave height maps for January during the years these two arrays were deployed have similar levels of ocean wave activity in this region. While it is possible that the NI region represents a common PP -wave bounce point from two separate sources, such an occurrence is highly unlikely because of the increased attenuation of PP waves. Several additional source regions are observed by the arrays but as these are not detected by two or more of the arrays for the month of January their provenance is less certain and we will not discuss them further here.

The June backprojection maps do not show any definitive P -wave microseism sources in the Northern Hemisphere, consistent with the reduction in northern extratropical cyclone activity in June. However, three of the arrays (Tanzania, Ethiopia and Cameroon) detected multiple sources of P -wave microseisms in the Southern Hemisphere. The lack of detection of these sources by the South Africa array is confirmed in other months and appears to be the result of strong slowness aliasing from the configuration of the array.

Both Ethiopia and Cameroon June backprojection spectra detect P waves from two regions in the 30° to 60° latitude belt of the Southern Hemisphere. One of these locations is near the plate boundary

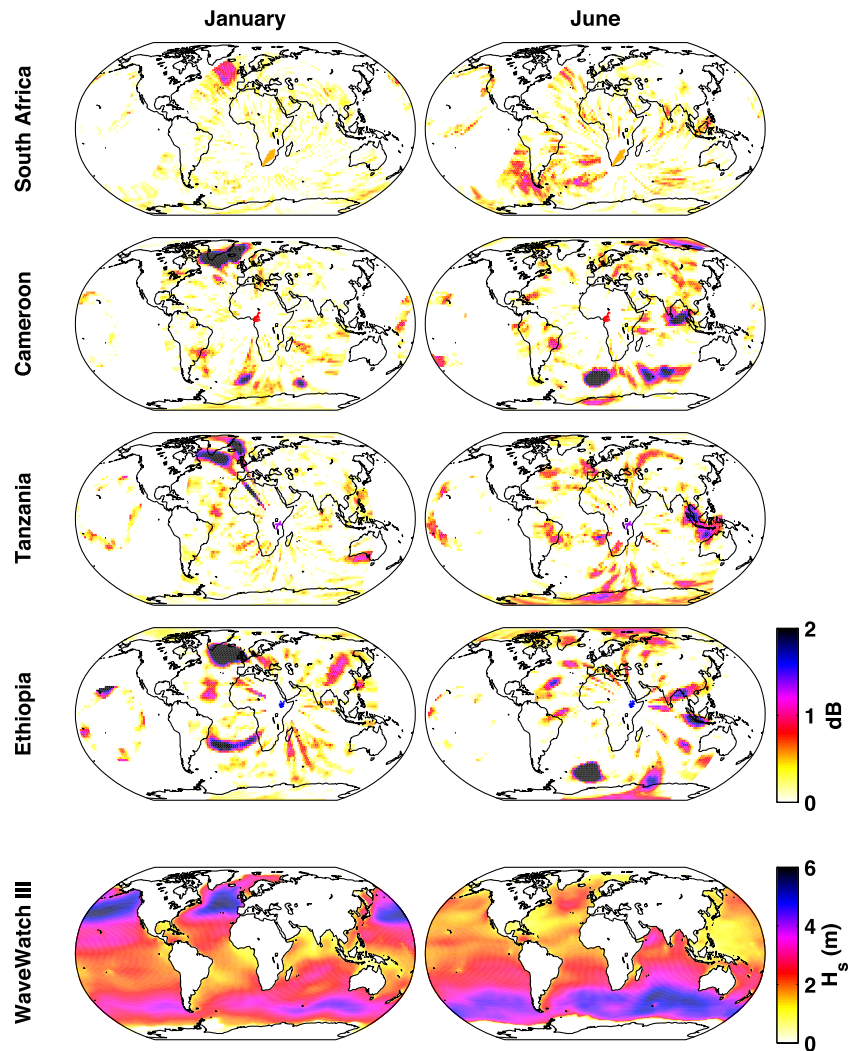


Figure 7. Seasonal comparison of P & PKP_{bc} backprojection of slowness spectra and WaveWatch III significant wave heights (Tolman 2009). The slowness spectra on the left are for each array in January averaged over the 5–7.5 s period band while the slowness spectra on the right are averaged for the month of June for the 7.5–10 s period band. The spectra are normalized to give 0 dB at the median value. Maps of significant wave heights from the WaveWatch III model are averaged over the months 2001 January and 2001 June.

triple-junction in the South Atlantic (SATJ). Bouvet island, which is the only island within this location, is small in area (49 km²) and unlikely to generate the ocean wave interference necessary to significantly excite teleseismic P -wave microseisms. Furthermore, the source region is much broader than the resolution at this location for either array (Fig. 5). This indicates that the P waves are generated over a broad region overlapping the plate boundary triple-junction and not just near the coast of Bouvet Island. We prefer to interpret the observations as the result of shallower bathymetry along the mid-ocean ridges near the SATJ enhancing the wave-interference coupling to the solid Earth. Arduin and Herbers (2013) extension of Longuet-Higgins (1950) theory of microseism generation indicates that specific ocean depths can have a substantial effect on P -wave excitation (see their fig. 11). An alternative explanation for the localization of P -wave microseisms that we did not explore is that extratropical cyclones travel faster in this region than in other parts of this belt which could generate a focused amount of wave interference (Haubrich & McCamy 1969).

The other source in the southern 30–60° latitude belt corresponds to P waves originating near the Kerguelen plateau (KP). This region has been noted by other studies as a significant source of body wave

microseisms (Gerstoft *et al.* 2008; Landes *et al.* 2010; Zhang *et al.* 2010a). This particular location likely represents the scenario for high amounts of microseism generation: regular storm activity over the local seas, increased wave interference from reflection off of the islands' coastlines and the enhancing effect of shallow bathymetry due to the KP.

The other generating region of June P -wave microseisms lies near the equator along the northern coast of the Indian Ocean extending from Southeast Asia to the northwest coast of Australia. This corresponds to the end of the monsoon season for Southeast Asia, but we do not observe an increase in the wave heights during adjacent months that would support this as an explanation for the P -wave microseism activity. If the microseisms were generated by the persistent interference of swell reflected along these coastlines, then the swells would have travelled from the southern Indian Ocean where they were generated by the extratropical cyclone activity which is relatively strong in June (Guo *et al.* 2009). In this case we would expect to observe similar microseismic activity during other months but we found that this region does not have P -wave microseism activity during any other month of the Southern Hemisphere winter season making this explanation less tenable. We have not

eliminated the possibility that these are the detection of earthquake activity such as an aftershock sequence, but this explanation also is unlikely as the arrays were not deployed contemporaneously and we have found little other evidence that would suggest earthquakes are influencing the f - s spectra.

4.2 Peak pick statistics

Overall, we picked 206 peaks in 96 f - s spectra from the four arrays using the procedure described earlier. While the SPDF and LPDF bands had similar totals, the number of peaks picked varied by array. Both the Tanzania and Cameroon arrays had nearly equal amounts of microseism detections in the two bands while the Ethiopia array detected nearly twice the LPDF sources compared to SPDF sources and the South Africa array mostly detected SPDF sources. Comparison of the slownesses of the f - s spectra picks finds ample P - and/or PP -wave sources while PKP phases account for <10 per cent of the picks (Fig. 8). This is consistent with relative amplitudes for these phases found by stacking many near-surface earthquakes (Astiz *et al.* 1996).

As noted in Section 3.3, the laterally heterogeneous structure of the Earth can bias the locations of the backprojected energy. We have investigated this effect for all peaks picked in the P -wave slowness range. The discrepancy between the uncorrected and corrected locations is typically less than 2°, but may be as much as 4° (Fig. 9a). This can affect the interpretation of P -wave microseism sources near the coast and should be performed for spectra that have resolution lengths smaller than this effect. The effect of the corrections on our SPDF P -wave source locations is generally minor, although we do note that the source locations to the southwest of Conrad Rise (CR) move closer to that feature. This may be the effect of the large, low shear velocity province in the lower mantle below Africa and also indicates that this source region may provide new constraints on that mantle structure. Repeating the correction procedure for velocity structure bias on the corrected locations gives similar slowness bias to the original locations (Fig. 9b) and confirms our assumption that the bias varies little over the scale lengths of the corrections and that the corrected locations are sufficient to account for the assumed velocity structure.

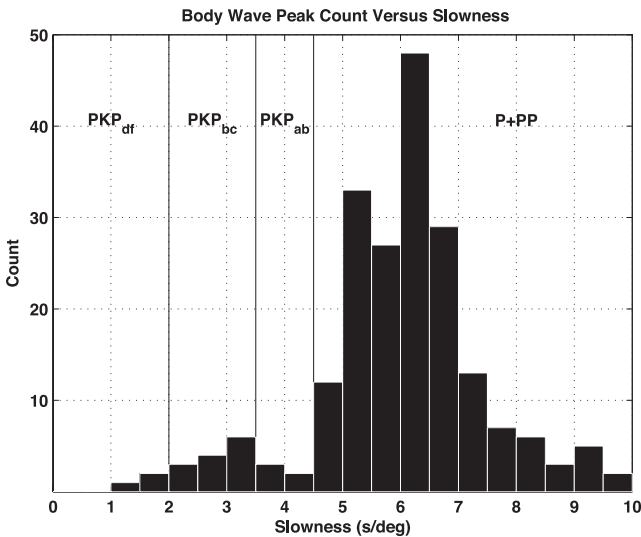


Figure 8. Number of picked peaks as a function of slowness with 0.5 s deg⁻¹ wide bins. Seismic phase slowness ranges are delimited by the solid vertical black lines and do not lie within any bins.

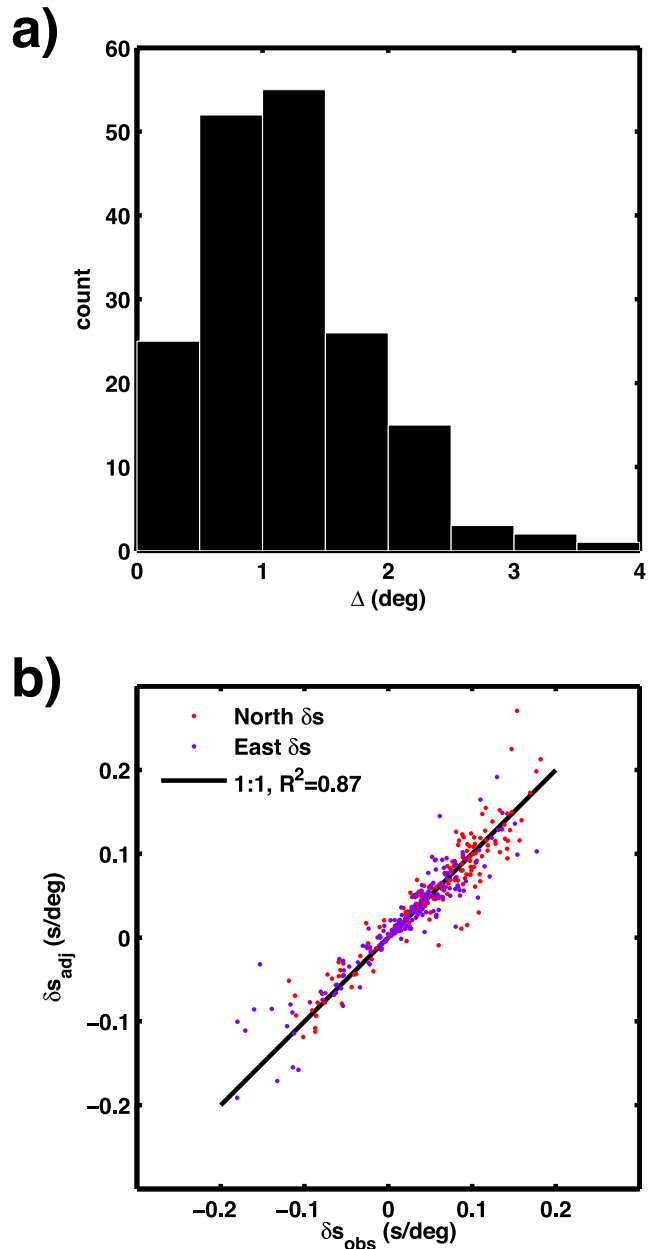


Figure 9. Correction of backprojected peak picks for 3-D seismic velocity heterogeneity by accounting for crustal (Laske *et al.* 2013) and mantle structure (Houser *et al.* 2008). (a) Histogram for all peaks in the P -wave slowness range binned by the distance between the uncorrected source location and the source location accounting for 3-D seismic velocity heterogeneity. (b) Comparison of the slowness bias caused by 3-D seismic velocity heterogeneity from the uncorrected (x -axis) and corrected (y -axis) locations.

By backprojecting and combining all of the SPDF or LPDF array picks in the P -wave slowness range onto a single map, we show that the rather complicated peak distribution in slowness space is simplified to a few geographic source regions (Fig. 10). In the Northern Hemisphere, the main source regions are the mid-Atlantic ridge extending South from Iceland (SI), near the southern tip of Greenland and the northern coast of Iceland (NI). In the Southern Hemisphere the source regions are the Walvis Ridge-Rio Grand Rise system (WR-RGR), the Antarctic Peninsula coastline (APC), the Enderby Abyss southeast of the CR, the plate boundary

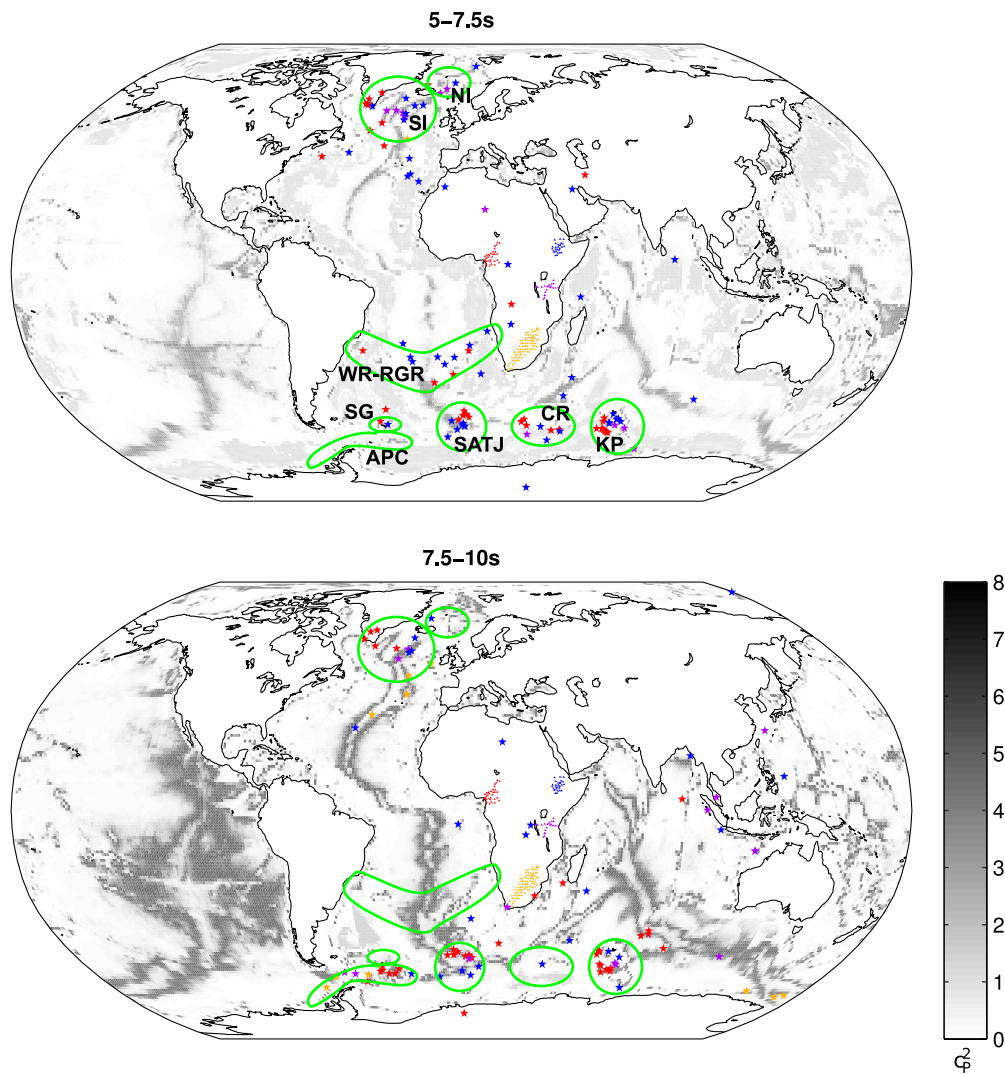


Figure 10. Backprojection of all peak picks (coloured stars) from periods (a) 5–7.5 s and (b) 7.5–10 s in the P -wave slowness range plotted on the P -wave bathymetric excitation coefficients for wave–wave interference (Ardhuin & Herbers 2013) for Crust1.0 (Laske *et al.* 2013). Star colouring corresponds to that of the observing array (triangles). Regions outlined in green denote the main body wave microseism source locations: north of Iceland (NI), south of Iceland (SI), Walvis Ridge-Rio Grande Rise (WR-RGR), South Georgia Island (SG), Antarctic Peninsula coast (APC), South Atlantic triple junction (SATJ), Conrad Rise (CR) and Kerguelen Plateau (KP).

triple-junction in the South Atlantic (SATJ) and the vicinity of South Georgia Island (SG) and the Kerguelen Plateau (KP).

The open ocean source regions in Fig. 10 (e.g. WR-RGR, SATJ and CR) may be explained by enhanced microseism generation in comparison to the surrounding regions due to the bathymetry (e.g. Longuet-Higgins 1950; Ardhuin & Herbers 2013) although the lack of detections of LPDF P -wave microseisms from two of these locations (WR-RGR and CR) is not in agreement with the expected increase in excitation from bathymetry. Alternative explanations for the lack of LPDF microseisms from these locations are related to consistent changes in storm speed and intensity as a function of position. For instance, this lack of detection may indicate that the speed of the storm exceeds the speed of the swell at SPDF periods but not at LPDF periods or that there is a lack of long-period ocean wave interference due to weaker storm systems. These are unlikely to explain the lack of LPDF P -waves from the CR region though as there are nearby source regions of LPDF P -wave microseisms at similar latitudes (e.g. SG, SATJ and KP). The APC source region only appears at LPDF periods and is also inconsistent

with the expected increase in bathymetric enhancement of microseism production at SPDF periods for this location. Recent work by Tanimoto (2007) and Gualtieri *et al.* (2013) has found that using a normal mode approach with more realistic Earth structure substantially changes the bathymetric excitation functions from those of Longuet-Higgins (1950) and Ardhuin & Herbers (2013). Thus these regions may require additional structural details to appropriately model their bathymetric excitation but we have not examined this possibility further.

The P -wave microseism detections originating from along the WR-RGR are a bit puzzling in that they are farther north than most of the Southern Hemisphere sources. There are some extratropical storm systems that pass near this latitude range of the South Atlantic but they are infrequent and typically occur in the Southern Hemisphere winter months. Fig. 7 indicates P -wave energy propagating across the Ethiopia array originating from this region during January (summer for the Southern Hemisphere) while a hindcast from this same time frame shows that the average significant wave heights over the region are among the lowest in the Southern

Table 1. Monthly *P*-wave peak pick counts combined from all four arrays for northerly ($N \pm 60^\circ$) and southerly ($S \pm 60^\circ$) azimuths.

	Jan	Feb	Mar	Apr	May	Jun	Jul	Aug	Sep	Oct	Nov	Dec	Total
North	12	9	3	2	0	0	4	1	1	1	9	8	50
South	7	8	10	11	10	12	14	9	11	10	9	6	117

Hemisphere. These observations could be explained if the WR-RGR is a region where wave–wave interaction far from storms like that observed by Obrebski *et al.* (2012) occurs frequently enough to have an influence at our timescales. The results of Arduin *et al.* (2011) do not support this theory though as the WR-RGR is found to not be a region of strong wave forcing over long time averages (this can be seen by looking at their fig. 7a). Another viable explanation for the WR-RGR *P*-wave microseisms is that the coupling of interfering waves in the region to the solid Earth is significantly enhanced by the local bathymetry in comparison to the surrounding regions. While this enhancement is not seen at SPDF periods where most of the detections occur, it is seen at LPDF periods (Fig. 10). We prefer this latter interpretation for the WR-RGR observations as the enhancement has a strong geographic correspondence to our observations, and seismic structure in this region may be influencing the frequency range of amplified *P*-wave microseism bathymetric excitation (e.g. Tanimoto 2007; Gualtieri *et al.* 2013).

Extratropical cyclones are strongest during the winter season of the hemisphere in which they are located. Comparison of the strength of the Northern and Southern hemisphere storm tracks shows that during the Northern Hemisphere winter the ratio is about unity while during the Southern Hemisphere winter the southern storm activity is about four times that of the north (e.g. Guo *et al.* 2009). Our limited monthly *P*-wave microseism source count agrees with these ratios (Table 1). However, the serendipitous effect of array location, source geometry and choices in averaging are likely to have had a significant influence on the observed ratio in microseism sources. Regardless, more comprehensive studies of microseisms may provide an independent measure of the relative strength of storms over the northern and southern oceans as the level of storm activity directly modulates the ocean wave spectrum and in turn the microseism spectrum.

5 DISCUSSION

5.1 Why no regional distance *P* waves?

One puzzling feature of this study is the reduction of body wave microseism sources at distances less than 60° . This can be seen in Fig. 8 as the rather significant difference in number of peaks picked at a slowness of 6 s deg^{-1} compared to 8 s deg^{-1} . Attenuation from the asthenosphere is not a reason for the lack of *PP* arrivals and *P* arrivals from shorter distances as the ray paths corresponding to slownesses below 10 s deg^{-1} extend into the lower mantle and thus do not spend a significant amount of time in the asthenosphere. One potential reason may be that the body waves propagating through the array from closer locations are poorly approximated by a plane wave and so their coherency is diminished in the *f*–*s* spectrum computation. Additionally, the slowness of *P* waves can vary substantially over the span of the arrays in this study, further reducing the coherency. Both of these may be avoided by beamforming directly for each location using delays based on the traveltimes to each receiver rather than a plane wave approximation across the array and backprojection of the result (e.g. Zhang *et al.* 2010a). A third effect,

similar to the previous two, is lateral variations in velocity structure. This can introduce phase delays that diminish coherency and bias the backprojection. Furthermore, the Tanzania and South Africa arrays are less effective in resolving body wave microseisms due to their unusual array responses (Fig. 3) so this could be a significant influence on the apparent lack of closer *P*-wave microseism sources as the arrays with more *P*-wave detections (Cameroon and Ethiopia) are further from the southern storm belt compared to the Tanzania and South Africa arrays.

5.2 Influence of bathymetry

Body wave microseisms are generally accepted to result from non-linear wave interference (Haubrich & McCamy 1969; Gerstoft *et al.* 2006; Zhang *et al.* 2009, 2010a; Obrebski *et al.* 2013). There are several ways that ocean waves interact to generate microseisms (Haubrich & McCamy 1969; Arduin *et al.* 2011): (1) reflection along the coasts, (2) interference directly under a storm, (3) in the wake of a storm or (4) between two storms. Studies of body wave microseisms in the secondary microseism frequency range (0.1–0.2 Hz) observed over short timescales have found that the body waves originate near tropical and extratropical storm tracks (Haubrich & McCamy 1969; Gerstoft *et al.* 2006, 2008; Zhang *et al.* 2010a,b; Obrebski *et al.* 2013). Statistical studies of microseisms at higher frequencies have observed body wave microseisms originating from the northern Pacific Ocean (Koper *et al.* 2009), the central Pacific Ocean (Koper & de Foy 2008; Koper *et al.* 2010) and the Central Atlantic (Koper & de Foy 2008). Zhang *et al.* (2009) found that seismic noise at similar high frequencies (0.6–2 Hz) has a significant amount of *P*-wave microseisms that are strongly correlated with offshore wind speeds.

In contrast to these studies of *P*-wave microseisms from short time windows, the source of 5–10 s microseismic body waves from averaging long time spans such as in our study are much more likely to originate within the extratropical cyclone belts at latitudes of 30 – 60° due to the persistent strong ocean wave activity in this region as evidenced by the significant wave height maps (Tolman 2009) in Figs 4 and 7. Our results for the Atlantic and Southern Oceans show that most of the *P*-wave sources are within the 30 – 60° latitude belts with some exceptions (e.g. the detections from the WR-RGR). This dominance of mid-latitude sources is in agreement with the 5–10 s period results of Landes *et al.* (2010) who used a technique similar to that of our study. This is also largely consistent with the survey of short time span body wave microseism sources found by Obrebski *et al.* (2013) who looked at ~ 0.2 Hz *P*-wave microseisms observed by the Southern California Seismic Network. They found that the microseismic *P* waves originated from the 30 – 60° latitude range in the northern and southern Pacific Ocean while a large number of sources were found at mid- and low latitudes in the North Atlantic.

Comparison of our results (Fig. 10) to the model of Arduin *et al.* (2011) find striking agreement to their 0.08–0.32 Hz Rayleigh wave microseismic source regions from a year-long average of wave–wave interference (e.g. see their fig. 7b) as we have found microseismic *P*-wave detection clusters for all of their seismic sources in

the North Atlantic, South Atlantic and Indian ocean. Our results only indicate one additional source missing from their model: the WR-RGR. This correspondence shows that averaging microseism data over long time spans can potentially lead to similar source distributions for Rayleigh waves and *P* waves, a feature which is not found by microseism studies looking at short time spans (e.g. Haubrich & McCamy 1969; Obrebski *et al.* 2013). The strong agreement of our source regions for multiple arrays across a broad time span suggests that static features such as bathymetry and seismic structure have strong control on the source locations of persistent body wave microseisms and that the relative amplitude of these sources are modulated by the seasonally varying intensity of the extratropical cyclone belts. These results show that the source regions for body wave microseisms from averages of a month or more of data can be readily inferred from averages of significant wave height (Tolman 2009) and the bathymetric amplification factor (Longuet-Higgins 1950; Arduin & Herbers 2013).

6 CONCLUSIONS

Using frequency-slowness analysis of multiple broad-band seismometer arrays, we show that monthly averages of body wave microseisms propagating through equatorial and southern Africa are largely consistent with locations predicted by microseism theory for their generation from wave–wave interference (Arduin *et al.* 2011; Arduin & Herbers 2013). The frequency dependence in these results shows that sources of SPDF (5–7.5 s) and LPDF (7.5–10 s) microseisms have substantial differences that imply that the bathymetry below the interference region plays a critical role in the excitation of body wave microseisms, corroborating previous theory (Longuet-Higgins 1950; Tanimoto 2007; Arduin & Herbers 2013). These variations with frequency provide a better source distribution that is potentially useful for seismic tomography studies. Corrections to our source locations for bias from seismic velocity structure show a potentially significant impact on our interpretation of some sources and should be accounted for in studies requiring high-resolution *P*-wave microseism source locations. Northern and Southern hemisphere body wave sources are consistent with the seasonality of extratropical cyclone activity and by comparing these regions we have shown that they can be useful for monitoring the relative strength of the two extratropical storm belts independent of satellite-based studies (e.g. Guo *et al.* 2009). The observed frequency-dependent behaviour of *P*-wave microseisms from the APC, CR and WR-RGR regions were found to be inconsistent with expectations based on bathymetric excitation (Arduin & Herbers 2013). These may be related to recent discrepancies noted in bathymetric excitation coefficients (Tanimoto 2007; Gualtieri *et al.* 2013) and warrant further investigation.

ACKNOWLEDGEMENTS

We thank the IRIS Data Management Center, PASSCAL and the numerous field crews for their hard work in providing excellent seismic data from the four temporary arrays in this study. We thank Gabi Laske, Christine Houser, Fabrice Arduin and the Marine Modelling and Analysis Branch at the Environmental Modeling Center of NOAA/NWS for making their models and codes available publicly. GE thanks Nicholas Harmon for help in improving our beamforming codes as well as Patrick Shore for his encouragement and guidance during the writing process. We appreciate the help of Anya Reading and an anonymous reviewer who improved the content of

this manuscript. This research was supported by the US National Science Foundation grants EAR-0310094 & EAR-0310272.

REFERENCES

- Arduin, F. & Herbers, T.H.C., 2013. Noise generation in the solid Earth, oceans and atmosphere, from nonlinear interacting surface gravity waves in finite depth, *J. Fluid Mech.*, **716**, 316–348.
- Arduin, F., Stutzmann, E., Schimmel, M. & Mangeney, A., 2011. Ocean wave sources of seismic noise, *J. geophys. Res.*, **116**, C09004, doi:10.1029/2011JC006952.
- Arduin, F., Balanche, A., Stutzmann, E. & Obrebski, M., 2012. From seismic noise to ocean wave parameters: general methods and validation, *J. geophys. Res.*, **117**, C05002, doi:10.1029/2011JC007449.
- Aster, R.C., McNamara, D.E. & Bromirski, P.D., 2008. Multidecadal climate-induced variability in microseisms, *Seismol. Res. Lett.*, **79**(2), 194–202.
- Aster, R.C., McNamara, D.E. & Bromirski, P.D., 2010. Global trends in extremal microseism intensity, *Geophys. Res. Lett.*, **37**, L14303, doi:10.1029/2010GL043472.
- Astiz, L., Earle, P.S. & Shearer, P.M., 1996. Global stacking of broadband seismograms, *Seismol. Res. Lett.*, **67**(4), 8–18.
- Backus, M., Burg, J., Baldwin, D. & Bryan, E., 1964. Wide-band extraction of mantle P waves from ambient noise, *Geophysics*, **29**(5), 672–692.
- Bastow, I.D., Nyblade, A.A., Stuart, G.W., Rooney, T.O. & Benoit, M.H., 2008. Upper mantle seismic structure beneath the Ethiopian hot spot: rifting at the edge of the African low-velocity anomaly, *Geochem. Geophys. Geosyst.*, **9**(12), Q12022, doi:10.1029/2008GC002107.
- Bengtsson, L., Hodges, K.I. & Keenlyside, N., 2009. Will extratropical storms intensify in a warmer climate? *J. Climate*, **22**, 2276–2301.
- Benson, G.D., Ritzwooller, M.H., Barmin, M.P., Levshin, A.L., Lin, F., Moschetti, M.P., Shapiro, N.M. & Yang, Y., 2007. Processing seismic ambient noise data to obtain reliable broad-band surface wave dispersion measurements, *Geophys. J. Int.*, **169**, 1239–1260.
- Brenguier, F., Campillo, M., Hadziioannou, C., Shapiro, N.M., Nadeau, R.M. & Larose, E., 2008a. Postseismic relaxation along the San Andreas fault at Parkfield from continuous seismological observations, *Science*, **321**, 1478–1481.
- Brenguier, F., Shapiro, N.M., Campillo, M., Ferrazzini, V., Duputel, Z., Coutant, O. & Nercessian, A., 2008b. Towards forecasting volcanic eruptions using seismic noise, *Nature Geosci.*, **1**(2), 126–130.
- Bromirski, P.D. & Duennebie, F.K., 2002. The near-coastal microseism spectrum: spatial and temporal wave climate relationships, *J. geophys. Res.*, **107**(B8), doi:10.1029/2001JB000265.
- Bromirski, P.D., Duennebie, F.K. & Stephen, R.A., 2005. Mid-ocean microseisms, *Geochem. Geophys. Geosyst.*, **6**(4), Q04009, doi:10.1029/2004GC000768.
- Burg, J.P., 1964. Three-dimensional filtering with an array of seismometers, *Geophysics*, **29**(5), 693–713.
- Capon, J., 1969. High-resolution frequency-wavenumber spectrum analysis, *Proc. IEEE*, **57**(8), 1408–1418.
- Capon, J., 1973. Analysis of microseismic noise at LASA, NORSAR, and ALPA, *Geophys. J. R. astr. Soc.*, **35**, 39–54.
- Cessaro, R.K., 1994. Sources of primary and secondary microseisms, *Bull. seism. Soc. Am.*, **84**(1), 142–148.
- Cessaro, R.K. & Chan, W.W., 1989. Wide-angle triangulation array study of simultaneous primary microseism sources, *J. geophys. Res.*, **94**(B11), 15 555–15 563.
- Chevrot, S., Sylvander, M., Benahmed, S., Ponsolles, C., Lefevre, J.M. & Paradis, D., 2007. Source locations of secondary microseisms in western Europe: evidence for both coastal and pelagic sources, *J. geophys. Res.*, **112**, B11301, doi:10.1029/2007JB005059.
- Dugda, M.T., Nyblade, A.A., Julià, J., Langston, C.A., Ammon, C.J. & Simiyu, S., 2005. Crustal structure in Ethiopia and Kenya from receiver function analysis: implications for rift development in eastern Africa, *J. geophys. Res.*, **110**, B01303, doi:10.1029/2004JB003065.

- Fouch, M.J., James, D.E., VanDecar, J.C. & van der Lee, S. Kaapvaal Seismic Group, 2004. Mantle seismic structure beneath the Kaapvaal and Zimbabwe Cratons, *S. Afr. J. Geol.*, **107**, 33–44.
- Friedrich, A., Kruger, F. & Klinge, K., 1998. Ocean-generated microseismic noise located with the Grafenberg array, *J. Seismol.*, **2**, 47–64.
- Gerstoft, P. & Tanimoto, T., 2007. A year of microseisms in southern California, *Geophys. Res. Lett.*, **34**, L20304, doi:10.1029/2007GL031091.
- Gerstoft, P., Fehler, M.C. & Sabra, K.G., 2006. When Katrina hit California, *Geophys. Res. Lett.*, **33**, L17308, doi:10.1029/2006GL027270.
- Gerstoft, P., Shearer, P.M., Harmon, N. & Zhang, J., 2008. Global P, PP, and PKP wave microseisms observed from distant storms, *Geophys. Res. Lett.*, **35**, L23306, doi:10.1029/2008GL036111.
- Grob, M., Maggi, A. & Stutzmann, E., 2011. Observations of the seasonality of the Antarctic microseismic signal, and its association to sea ice variability, *Geophys. Res. Lett.*, **38**, L11302, doi:10.1029/2011GL047525.
- Gualtieri, L., Stutzmann, E., Capdeville, Y., Arduin, F., Schimmel, M., Mangeny, A. & Morelli, A., 2013. Modeling secondary microseismic noise by normal mode summation, *Geophys. J. Int.*, **193**, 1732–1745.
- Guo, Y., Chang, E.K.M. & Leroy, S.S., 2009. How strong are the southern hemisphere storm tracks? *Geophys. Res. Lett.*, **36**, L22806, doi:10.1029/2009GL040733.
- Harmon, N., Rychert, C. & Gerstoft, P., 2010. Distribution of noise sources for seismic interferometry, *Geophys. J. Int.*, **183**, 1470–1484.
- Hasselmann, K., 1963. A statistical analysis of the generation of microseisms, *Rev. Geophys.*, **1**(2), 177–210.
- Haubrich, F.A., 1968. Array design, *Bull. seism. Soc. Am.*, **58**(3), 977–991.
- Haubrich, F.A. & McCamy, K., 1969. Microseisms: coastal and pelagic sources, *Rev. Geophys.*, **7**(3), 539–571.
- Haubrich, R.A., Munk, W.H. & Snodgrass, F.E., 1963. Comparative spectra of microseisms and swell, *Bull. seism. Soc. Am.*, **53**(1), 27–37.
- Houser, C., Masters, G., Shearer, P. & Laske, G., 2008. Shear and compressional velocity models of the mantle from cluster analysis of long-period waveforms, *Geophys. J. Int.*, **174**(1), 195–212.
- James, D.E., Fouch, M.J., VanDecar, J.C. & van der Lee, S. Kaapvaal Seismic Group, 2001. Tectospheric structure beneath southern Africa, *Geophys. Res. Lett.*, **28**(13), 2485–2488.
- James, D.E., Niu, F. & Rokosky, J., 2003. Crustal structure of the Kaapvaal craton and its significance for early crustal evolution, *Lithos*, **71**, 413–429.
- Julià, J., Ammon, C.J. & Nyblade, A.A., 2005. Evidence for mafic lower crust in Tanzania, East Africa, from joint inversion of receiver functions and Rayleigh wave dispersion velocities, *Geophys. J. Int.*, **162**, 555–569.
- Kedar, S., Longuet-Higgins, M., Webb, F., Graham, N., Clayton, R. & Jones, C., 2008. The origin of deep ocean microseisms in the North Atlantic Ocean, *Proc. R. Soc. A*, **464**, 777–793.
- Kennett, B.L.N. & Gudmundsson, O., 1996. Ellipticity corrections for seismic phases, *Geophys. J. Int.*, **127**, 40–48.
- Kennett, B.L.N., Engdahl, E.R. & Buland, R., 1995. Constraints on seismic velocities in the Earth from travel times, *Geophys. J. Int.*, **122**, 108–124.
- Kim, S., Nyblade, A.A., Rhie, J., Baag, C.-E. & Kang, T.-S., 2012. Crustal S-wave velocity structure of the Main Ethiopian Rift from ambient noise tomography, *Geophys. J. Int.*, **191**, 865–878.
- Koch, F.W., Wiens, D.A., Nyblade, A.A., Shore, P.J., Tibi, R., Ateba, B., Tabod, C.T. & Nnange, J.M., 2012. Upper-mantle anisotropy beneath the Cameroon volcanic line and Congo craton from shear wave splitting measurements, *Geophys. J. Int.*, **190**(1), 75–86.
- Koper, K.D. & de Foy, B., 2008. Seasonal anisotropy in short-period seismic noise recorded in South Asia, *Bull. seism. Soc. Am.*, **98**(6), 3033–3045.
- Koper, K.D., de Foy, B. & Benz, H., 2009. Composition and variation of noise recorded at the Yellowknife seismic array, 1991–2007, *J. geophys. Res.*, **114**, B10310, doi:10.1029/2009JB006307.
- Koper, K.D., Seats, K. & Benz, H.M., 2010. On the composition of Earth's short period seismic noise field, *Bull. seism. Soc. Am.*, **100**(2), 606–617.
- Lacoss, R.T., Kelly, E.J. & Toksöz, N.M., 1969. Estimation of seismic noise structure using arrays, *Geophysics*, **34**(1), 21–38.
- Landes, M., Hubans, F., Shapiro, N.M., Paul, A. & Campillo, M., 2010. Origin of deep ocean microseisms by using teleseismic body waves, *J. geophys. Res.*, **115**, B05302, doi:10.1029/2009JB006918.
- Laske, G., Masters, G., Ma, Z. & Pasayanos, M., 2013. Update on CRUST1.0: a 1-degree global model of Earth's crust, *Geophys. Res. Abstr.*, **15**, Abstract EGU2013-2658.
- Lawrence, J.F. & Prieto, G.A., 2011. Attenuation tomography in the western United States from ambient seismic noise, *J. geophys. Res.*, **116**, B06302, doi:10.1029/2010JB007836.
- Lin, F.-C. & Ritzwoller, M.H., 2011. Helmholtz surface wave tomography for isotropic and azimuthally anisotropic structure, *Geophys. J. Int.*, **186**, 1104–1120.
- Lin, F.-C., Moschetti, M.P. & Ritzwoller, M.H., 2008. Surface wave tomography of the western United States from ambient seismic noise: Rayleigh and Love wave phase velocity maps, *Geophys. J. Int.*, **173**, 281–298.
- Lin, F.-C., Ritzwoller, M.H. & Snieder, R., 2009. Eikonal tomography: surface wave tomography by phase front tracking across a regional broadband seismic array, *Geophys. J. Int.*, **177**, 1091–1110.
- Lin, F.-C., Schmandt, B. & Tsai, V.C., 2012a. Joint inversion of Rayleigh wave phase velocity and ellipticity using USArray: constraining velocity and density structure in the upper crust, *Geophys. Res. Lett.*, **39**, L12303, doi:10.1029/2012GL052196.
- Lin, F.-C., Tsai, V.C. & Ritzwoller, M. H., 2012b. The local amplification of surface waves: a new observable to constrain elastic velocities, density, and anelastic attenuation, *J. geophys. Res.*, **117**, B06302, doi:10.1029/2012JB009208.
- Longuet-Higgins, M.S., 1950. A theory of the origin of microseisms, *Phil. Trans. R. Soc. Lond. A*, **243**(857), 1–35.
- Lorenz, E. N., 1955. Available potential energy and the maintenance of the general circulation, *Tellus*, **7**, 157–167.
- McNamara, D.E. & Buland, R.P., 2004. Ambient noise levels in the continental United States, *Bull. seism. Soc. Am.*, **94**(4), 1517–1527.
- Nolet, G., 2008. *A Breviary of Seismic Tomography: Imaging the Interior of the Earth and Sun*, Cambridge Univ. Press, 344 p.
- Nyblade, A.A. & Langston, C.A., 2002. Broadband seismic experiments probe the East African Rift, *EOS, Trans. Am. geophys. Un.*, **83**(37), doi:10.1029/2002EO000296.
- Nyblade, A.A., Birt, C., Langston, C.A., Owens, T.J. & Last, R.J., 1996. Seismic experiment reveals rifting of craton in Tanzania, *EOS, Trans. Am. geophys. Un.*, **77**(51), 517–519.
- Obrebski, M.J., Arduin, F., Stutzmann, E. & Schimmel, M., 2012. How moderate sea states can generate loud seismic noise in the deep ocean, *Geophys. Res. Lett.*, **39**, L11601, doi:10.1029/2012GL051896.
- Obrebski, M., Arduin, F., Stutzmann, E. & Schimmel, M., 2013. Detection of microseismic compressional (P) body waves aided by numerical modeling of oceanic noise sources, *J. geophys. Res.*, **118**, 4312–4324.
- Peterson, J., 1993. Observation and modeling of seismic background noise, *Tech. Rep. U.S. Geol. Surv.*, 93-322, I-95.
- Prieto, G.A., Lawrence, J.F. & Beroza, G.C., 2009. Anelastic Earth structure from the coherency of the ambient seismic field, *J. geophys. Res.*, **114**, B07303, doi:10.1029/2008JB006067.
- Ramirez, J.E., 1940a. An experimental investigation of the nature and origin of microseisms at St. Louis, Missouri: part one, *Bull. seism. Soc. Am.*, **30**(1), 35–84.
- Ramirez, J.E., 1940b. An experimental investigation of the nature and origin of microseisms at St. Louis, Missouri: part two, *Bull. seism. Soc. Am.*, **30**(2), 139–178.
- Reusch, A.M., Nyblade, A.A., Wiens, D.A., Shore, P.J., Ateba, B., Tabod, C.T. & Nnange, J.M., 2010. Upper mantle structure beneath Cameroon from body wave tomography and the origin of the Cameroon volcanic line, *Geochem. Geophys. Geosyst.*, **11**, Q10W07, doi:10.1029/2010GC003200.
- Reusch, A.M., Nyblade, A.A., Tibi, R., Wiens, D.A., Shore, P.J., Bekoa, A., Tabod, C.T. & Nnange, J.M., 2011. Mantle transition zone thickness beneath Cameroon: evidence for an upper mantle origin for the Cameroon volcanic line, *Geophys. J. Int.*, **187**, 1146–1150.
- Rost, S. & Thomas, C., 2002. Array seismology: methods and applications, *Rev. Geophys.*, **40**(3), 1008–1034.
- Rost, S. & Thomas, C., 2009. Improving seismic resolution through array processing techniques, *Surv. Geophys.*, **30**, 271–299.

- Sabra, K.G., Gerstoft, P., Roux, P., Kuperman, W.A. & Fehler, M.C., 2005. Extracting time-domain Green's function estimates from ambient seismic noise, *Geophys. Res. Lett.*, **32**, L03310, doi:10.1029/2004GL021862.
- Schulte-Pelkum, V., Earle, P.S. & Vernon, F.L., 2004. Strong directivity of ocean-generated seismic noise, *Geochem. Geophys. Geosyst.*, **5**(3), Q03004, doi:10.1029/2003GC000520.
- Seatz, K.J., Lawrence, J.F. & Prieto, G.A., 2012. Improved ambient noise correlation functions using Welch's method, *Geophys. J. Int.*, **188**, 513–523.
- Sens-Schönfelder, C. & Wegler, U., 2006. Passive image interferometry and seasonal variations of seismic velocities at Merapi Volcano, Indonesia, *Geophys. Res. Lett.*, **33**, L21302, doi:10.1029/2006GL027797.
- Shapiro, N.M., Ritzwoller, M.H. & Bensen, G.D., 2006. Source location of the 26 sec microseism from cross-correlations of ambient seismic noise, *Geophys. Res. Lett.*, **33**, L18310, doi:10.1029/2006GL027010.
- Sheen, D.-H., Shin, J.S., Kang, T.-S. & Baag, C.-E., 2009. Low frequency cultural noise, *Geophys. Res. Lett.*, **36**, L17314, doi:10.1029/2009GL039625.
- Stehly, L., Campillo, M. & Shapiro, N.M., 2006. A study of the seismic noise from its long-range correlation properties, *J. geophys. Res.*, **111**, B10306, doi:10.1029/2005JB004237.
- Stutzmann, E., Schimmel, M., Patau, G. & Maggi, A., 2009. Global climate imprint on seismic noise, *Geochem. Geophys. Geosyst.*, **10**(11), Q11004, doi:10.1029/2009GC002619.
- Tanimoto, T., 2007. Excitation of microseisms, *Geophys. Res. Lett.*, **34**, L05308, doi:10.1029/2006GL029046.
- Tokam, A.K., Tabod, C.T., Nyblade, A.A., Julià, J., Wiens, D.A. & Pasyanos, M.E., 2010. Structure of the crust beneath Cameroon, West Africa, from the joint inversion of Rayleigh wave group velocities and receiver functions, *Geophys. J. Int.*, **183**(2), 1061–1076.
- Toksöz, M.N. & Lacoss, R.T., 1968. Microseisms: mode structure and sources, *Science*, **159**(3817), 872–873.
- Tolman, H.L., 2009. *User manual and system documentation of WAVEWATCH III version 3.14. NOAA/NWS/NCP/MMAB Technical Note 276.*
- Tsai, V.C., 2009. On establishing the accuracy of noise tomography travel-time measurements in a realistic medium, *Geophys. J. Int.*, **178**, 1555–1564.
- Wallace, J.M. & Hobbs, P.V., 2006. *Atmospheric Science: An Introductory Survey*, 2nd edn, Academic Press, 504 pp.
- Webb, S.C., 1992. The equilibrium oceanic microseism spectrum, *J. acoust. Soc. Am.*, **92**(4-1), 2141–2158.
- Webb, S.C., 2008. The Earth's hum: the excitation of Earth normal modes by ocean waves, *Geophys. J. Int.*, **174**, 542–566.
- Weeraratne, D.S., Forsyth, D.W., Fischer, K.M. & Nyblade, A.A., 2003. Evidence for an upper mantle plume beneath the Tanzanian craton from Rayleigh wave tomography, *J. geophys. Res.*, **108**, B92427, doi:10.1029/2002JB002273.
- Wegler, U. & Sens-Schönfelder, C., 2007. Fault zone monitoring with passive image interferometry, *Geophys. J. Int.*, **168**, 1029–1033.
- Welch, P.D., 1967. The use of fast Fourier transform for the estimation of power spectra: a method based on time averaging over short, modified periodograms, *IEEE Trans. Audio Electroacoust.*, **AU-15**, 70–73.
- Westwood, E.K., 1992. Broadband matched-field source localization, *J. acoust. Soc. Am.*, **91**(5), 2777–2789.
- Yang, Y. & Ritzwoller, M.H., 2008. Characteristics of ambient seismic noise as a source for surface wave tomography, *Geochem. Geophys. Geosyst.*, **9**(2), doi:10.1029/2007GC001814.
- Yang, Y., Li, A. & Ritzwoller, M.H., 2008. Crustal and uppermost mantle structure in southern Africa from ambient noise and teleseismic tomography, *Geophys. J. Int.*, **174**(1), 235–248.
- Zhang, J., Gerstoft, P. & Shearer, P.M., 2009. High-frequency P-wave seismic noise driven by ocean winds, *Geophys. Res. Lett.*, **36**, L09302, doi:10.1029/2009GL037761.
- Zhang, J., Gerstoft, P. & Bromirski, P.D., 2010a. Pelagic and coastal sources of P-wave microseisms: generation under tropical cyclones, *Geophys. Res. Lett.*, **37**, L15301, doi:10.1029/2010GL044288.
- Zhang, J., Gerstoft, P. & Shearer, P.M., 2010b. Resolving P-wave travel-time anomalies using seismic array observations of oceanic storms, *Earth Planet. Sci. Lett.*, **292**, 419–427.